İSTANBUL UNIVERSITY CERRAHPAŞA

ORIGINAL ARTICLE
Electrica 2025; 25: 1-15

Experimental Investigation of SiC MOSFET-Based Isolated Dual Active Half-Bridge Converter: Hard-Switching Versus Soft-Switching

Veera Venkata Subrahmanya Kumar Bhajana[1], Pravat Biswal[1], Pavel Drabek[2], Vijay Kakani[3]

[1]School of Electronics Engineering, Kalinga Institute of Industrial Technology (KIIT), University, Bhubaneswar, India
[2]Regional Innovation Centre for Electrical Engineering, University of West Bohemia in Pilsen, Plzeň-30614, Czech Republic
[3]Department of Integrated System Engineering, Inha University School of Global Convergence Studies, Incheon, South Korea

Cite this article as: V. Venkata Subrahmanya Kumar Bhajana, P. Biswal, P. Drabek and V. Kakani, "Experimental investigation of SiC MOSFET-based isolated dual active half-bridge converter: hard-switching versus soft-switching," *Electrica*, 25, 0183, 2025. doi: 10.5152/electrica.2025.24183.

WHAT IS ALREADY KNOWN ON THIS TOPIC?

- *The Dual Active Bridge (DAB) converter is a popular isolated DC-DC topology known for bidirectional power flow and galvanic isolation, making it suitable for electric vehicle (EV) charging, renewable energy systems, and battery energy storage.*
- *Silicon Carbide (SiC) MOSFETs are well known for their superior performance compared to traditional silicon (Si) devices. They offer higher switching frequencies, lower conduction and switching losses, and improved thermal performance, which makes them ideal for high-efficiency and high-power-density converter applications*

Corresponding author:
Veera Venkata Subrahmanya Kumar Bhajana

E-mail:
bvvs.kumarfet|@kiit.ac.in

Received: November 26, 2024
Revision Requested: January 10, 2025
Last Revision Received: February 25, 2025
Accepted: March 17, 2025
Publication Date: May 20, 2025

DOI: 10.5152/electrica.2025.24183

ABSTRACT

This article presents the performance evaluation of an isolated dual active half-bridge (DAHB) converter with discrete SiC MOSFET devices. The impact of a resonant network on the SiC MOSFET DAHB under two different modes is investigated. The soft-switching characteristics, zero voltage switching (ZVS), and zero current switching (ZCS) operations are achieved by using a series resonant network. Another advantage of this DAHB converter without a resonant network is that it achieved partial soft switching for the main SiC MOSFETs. The discrete switching devices, SiC MOSFETs, are used to develop the DAHB module. The experimental investigations were performed on a DAHB converter system with 330V–500V switching frequency, 100 kHz operated at 700W output power, and obtained 96.5% efficiency.

Index Terms—Dual Half Bridge (DHB), isolated converter, resonant network, zero current switching (ZCS), zero voltage switching (ZVS)

I. INTRODUCTION

Nowadays, the performance of SiC and GaN devices presents an attractive solution for researchers aiming to develop more efficient converters. In energy storage systems (ESS), Dual Active Full Bridge (DAB) converters [1, 2] and Dual Active Half Bridge (DAHB) converters [3] play a crucial role in delivering the desired voltages and are recommended for operation at high power levels. To mitigate voltage fluctuations across the capacitors, an asymmetric charging method was introduced in a dual half-bridge (DHB) converter [4] using Si IGBTs. This control technique adjusts the switching times of the secondary-side switching devices, effectively resolving the voltage imbalance issue. In hybrid energy storage systems, a voltage balance algorithm has been developed [5] to regulate the primary-side currents and equalize the voltage on the secondary side. Additionally, power loop control is employed in the dual half-bridge (DHB) converter to minimize currents and adjust the duty cycles [6]. Similarly, an advanced control technique is employed to drive the current error through the primary side of the transformer in the DHB converter to zero [7]. To reduce the overall volume of the DHB and enhance its ability to withstand high power, an alternative approach is implemented by replacing the in-built capacitors, which may eliminate the need for input and output filters in DHBs [8]. To enhance fault-handling capability, reduce the size of large DC capacitors, and eliminate the need for a circuit breaker in the DAB, the input and output filters are replaced with half-bridge submodules [9]. However, the addition of extra switching devices may increase both the overall cost and size. Interleaved dual half-bridge converters [10, 11], coupled with DC split capacitors, have been shown to reduce the number of filter capacitors required. This represents an improvement in the isolated dual active half-bridge (DAB) converter, featuring lower voltage stresses and reduced current ripples. To minimize turn-on and turn-off losses and enhance the efficiency of the DAB converter [12], a combination of single-phase shift and variable frequency control techniques is employed. This approach allows for better management

WHAT THIS STUDY ADDS ON THIS TOPIC?

- *This Study focuses on discrete SiC MOSFETs, providing practical insights into their behavior and switching characteristics in an isolated DAHB topology.*
- *The study demonstrates a simple and effective method for achieving both Zero Voltage Switching (ZVS) and Zero Current Switching (ZCS) using basic LLC resonant components, eliminating the need for complex auxiliary circuits. This simplifies the design while retaining soft-switching benefits.*
- *The converter is experimentally tested under both hard- and soft-switching conditions, with direct comparison of switching losses, efficiency, and device stress. This provides clear performance benchmarks under realistic conditions.*

of switching transitions, reducing losses and improving overall performance, especially under varying load conditions. A solid-state transformer-based hybrid converter [13] is implemented with a half-bridge configuration on the primary side and a full-bridge configuration on the secondary side. This design reduces the total device count, enhances power density, and minimizes power pulsations at double the line frequency. To ensure smooth transitions between constant current and constant voltage charging modes, a feed-forward control strategy is implemented in the DAB converter [14]. Additionally, a three-loop control scheme is adopted, replacing the conventional two-loop approach, to optimally determine both the internal and external phase shift angles while also minimizing peak input current. Furthermore, DAB converters are enhanced by incorporating two three-level neutral-point-clamped (NPC) converters [15] on both sides. This approach helps balance the voltage clamping across all switching devices and facilitates soft-switching conditions, thereby improving overall efficiency and reducing switching losses. To reduce peak input current, and conduction losses, and enable direct power transfer, a coupled inductor-based four-level flying capacitor converter is implemented on the primary side [16], while a half-bridge configuration is used on the secondary side. To minimize the number of active devices in a dual active half bridge converter, a semi-active half-bridge DC-DC converter [17] is implemented. In addition, an advanced control strategy based on Voltage-Match Trapezoidal Modulation (VM-TZM) is employed to reduce peak current and ensure Zero Voltage Switching (ZVS) during the turn-on of all switches. A triple-phase shift control technique is implemented in the dual active half-bridge converter [18] to mitigate current stress and enable optimal duty cycle selection, thereby enhancing efficiency and reducing thermal losses. This technique facilitates improved power transfer by precisely managing the phase shift between the primary and secondary sides, contributing to reduced electromagnetic interference (EMI) and ensuring more stable operation under varying load conditions. To reduce the circulating power between two ports, a three-leg converter is employed on the secondary side, while two Dual Active Half-Bridge (DAHB) converters [19] are connected to different voltage sources. This configuration allows for more efficient power transfer, as the three-leg converter helps balance the power flow and minimize the losses associated with circulating currents. Additionally, the use of separate voltage sources for each DAHB converter provides better control over the energy distribution, enhancing overall system stability and performance under varying load conditions. Recently, SiC MOSFETs have emerged as an alternative solution for researchers seeking better efficiency and the capability to handle high power transfer. The performance of a SiC MOSFET-based dual half-bridge converter, implemented with a series resonant network, and the effects of small variations in phase shift angles have been reported in [20]. However, the performance analysis presented in the study is based on low input voltages and operates at very low power levels. Minimizing overall volume, reducing cost, and enhancing efficiency are critical challenges in the design of isolated DC-DC converters. This article primarily investigates the application of SiC MOSFETs as discrete switching devices in a dual active half-bridge (DAHB) converter, coupled with the integration of a series resonant network. Beyond exploring various control strategies, the focus of this paper is on evaluating the performance of the DAHB converter when employing discrete SiC MOSFETs, in contrast to using SiC power modules. The overall cost of the DAHB converter

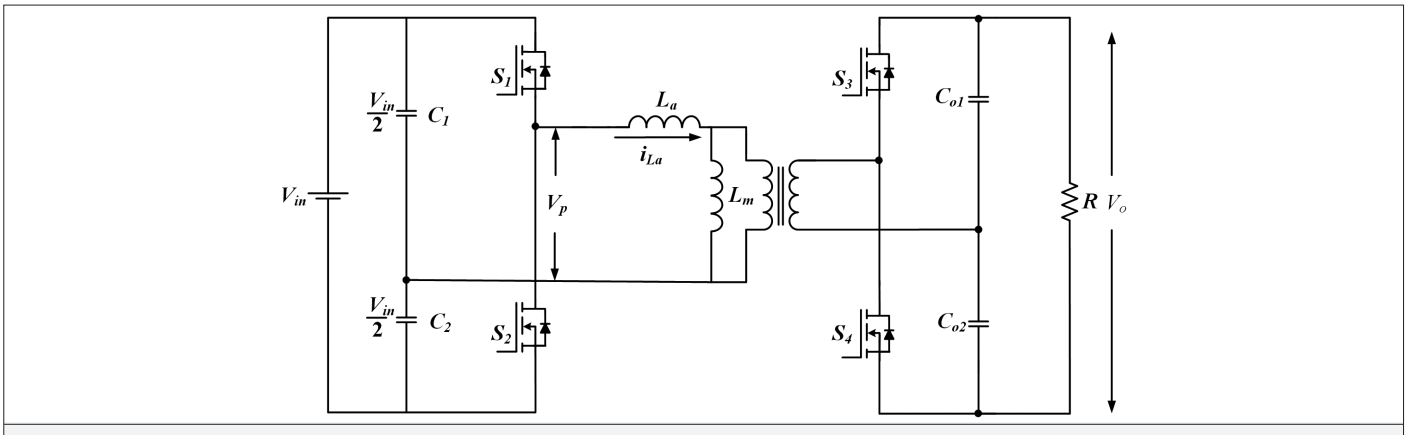

Fig. 1. SiC MOSFET-based dual active half bridge DC-DC converter.

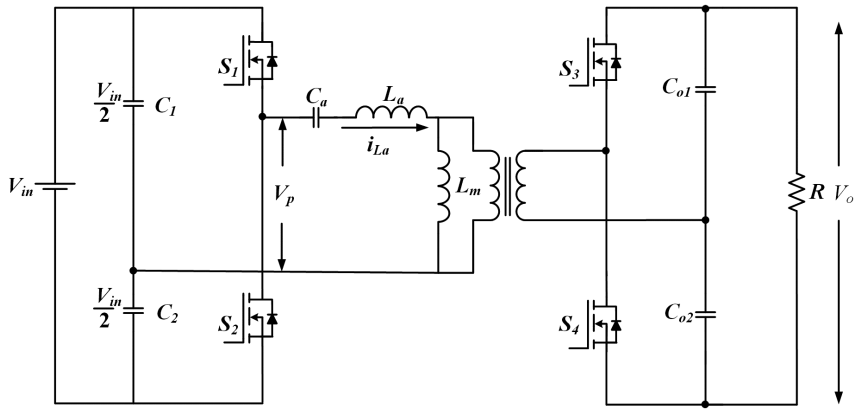

Fig. 2. SiC MOSFET-based LLC (Schematic of the LLC Resonant Dual Active Half-Bridge DC-DC Converter Utilizing Discrete SiC MOSFETs, Featuring Series Resonant Inductor (La),Magnetizing Inductance (Lm), , and Resonant Capacitor (Ca)) dual active half bridge DC-DC converter.

using discrete SiC MOSFETs is reduced by approximately 50% compared to the configuration using SiC power modules. This paper is organized as follows: section II describes the operating principles, section III presents design analysis, section IV presents the simulation analysis, and section V presents the experimental results.

II. DESCRIPTION AND OPERATION PRINCIPLES OF DUAL ACTIVE HALF-BRIDGE CONVERTER

The configuration of the dual active half-bridge (DAHB) converter, shown in Fig. 1 is with two active half-bridges isolated through a

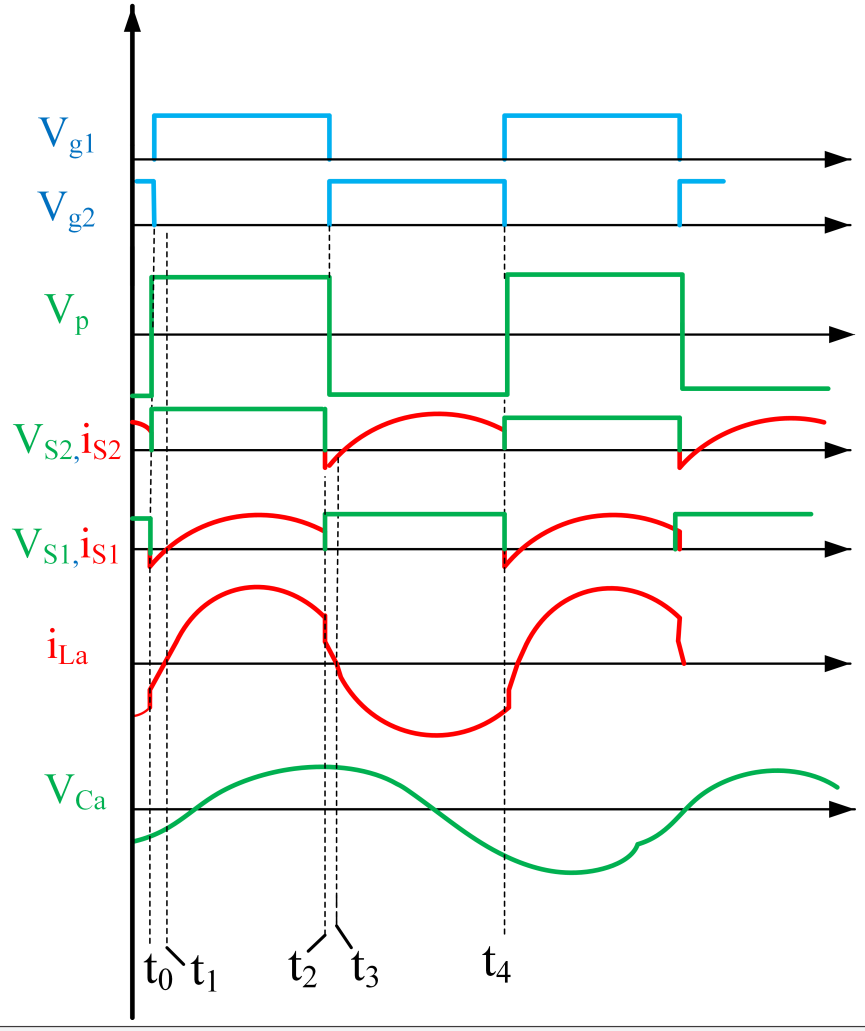

Fig. 3. Key waveforms: ZVS mode.

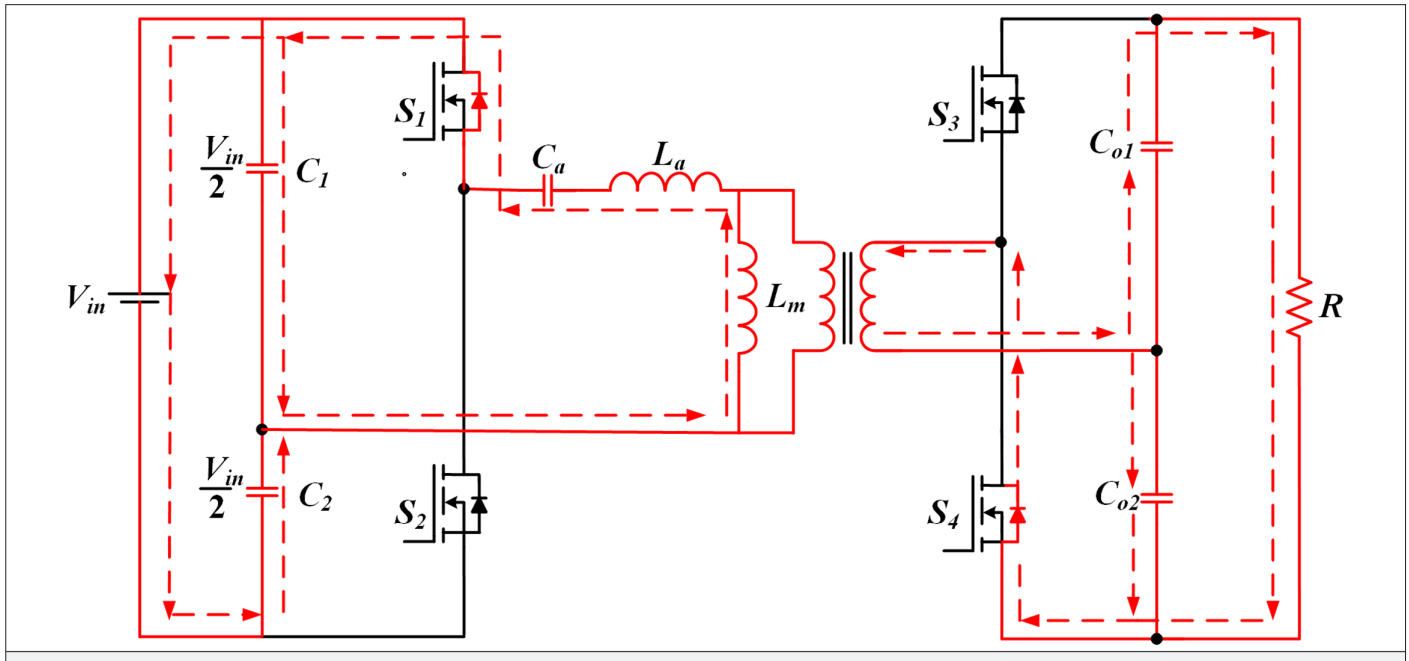

Fig. 4. Equivalent current flow schematic: Interval (t_0-t_1).

transformer. The primary side comprises two input capacitors, C_1, C_2, SiC MOSFETs, S_1, S_2. The secondary side is assisted with two SiC MOSFETs, S_3 *and* S_4, and output capacitors, C_{o1} and C_{o2}. Fig. 1 shows the DAHB converter with a series inductor L_a is the conventional DAHB with SiC MOSFETs, which have more switching losses. To incorporate soft-switching features into SiC MOSFETs, a resonant network is adopted. Fig. 2 shows the DAHB primary side included with additional components: a series resonant inductor, L_a, a series resonant capacitor, C_a, and a magnetizing inductance, L_m. The DAHB converter operates in two modes. The first mode occurs when the switching frequency is higher than the resonant frequency, known as the zero voltage switching (ZVS) mode, and the second mode, when the switching frequency is less than the resonant frequency, is known as zero current switching (ZCS) mode. The operation is divided into four intervals based on the key waveforms shown in Figs. 3 and 4, Figs. 5-7 shows the equivalent circuits of all the intervals from t_0-t_4.

A. Zero Voltage Switching Mode

Interval (t_0-t_1): This interval begins when S_1, S_4 are gated, primary side voltage, V_P, clamps to the $nV_o/2$ and resonant current, i_{La} flows through the body diodes of S_1, S_4. Hence the ZVS condition is achieved for S_1, S_4. At t_1, body diodes of S_1, S_4 stop conducting.

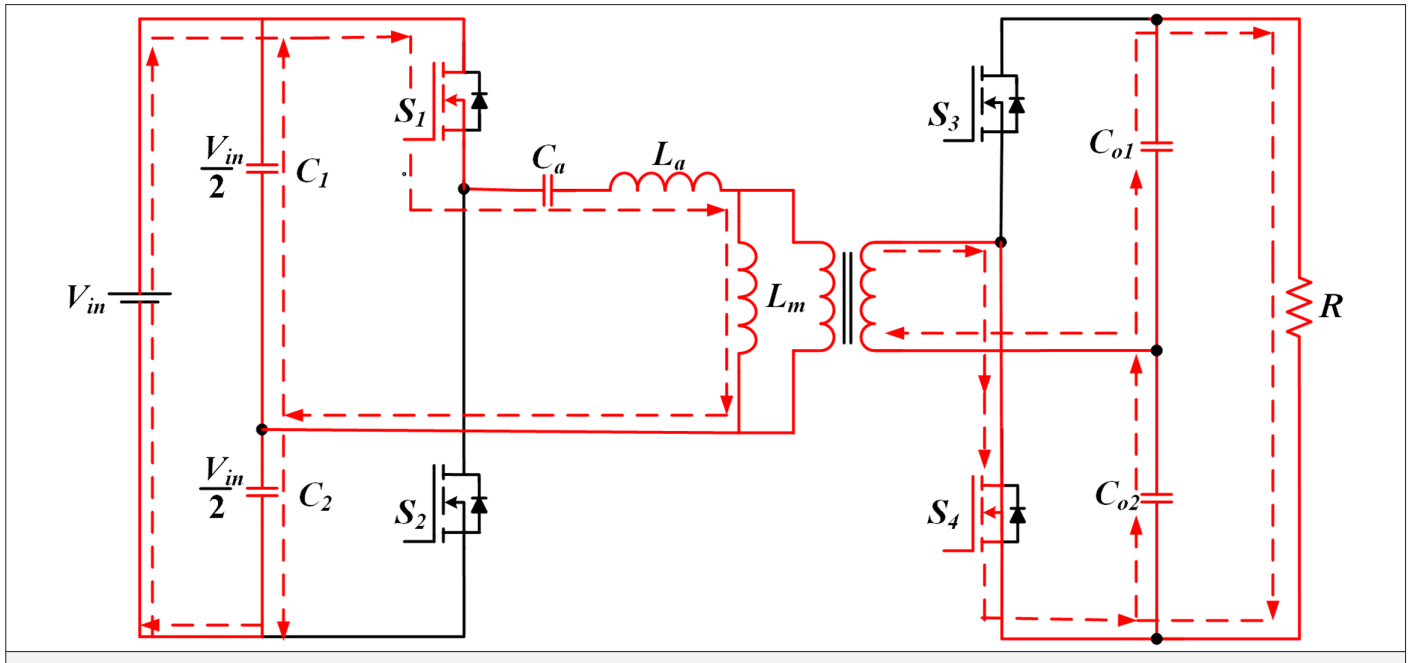

Fig. 5. Equivalent current flow schematic: Interval (t_1-t_2).

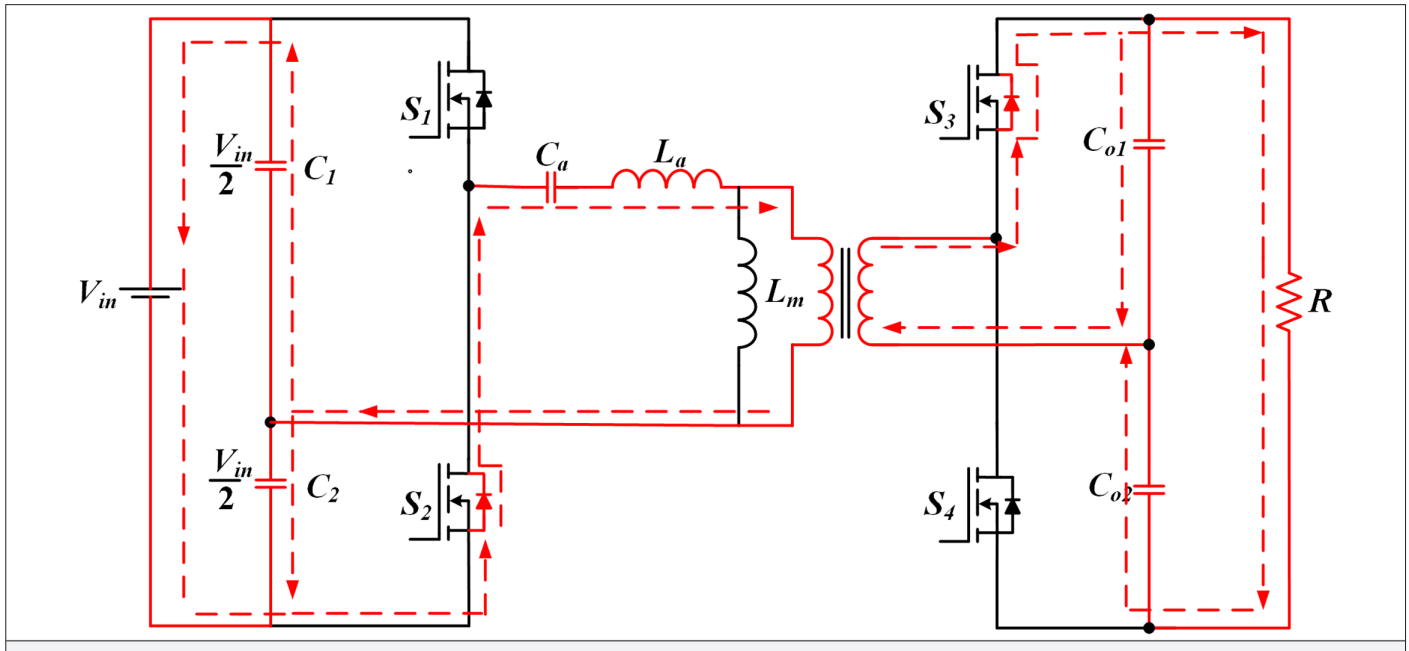

Fig. 6. Equivalent current flow schematic: Interval (t_2-t_3).

The resonant current, i_{La}, and voltage across the capacitor, C_a, are expressed in (1) and (2).

$$i_{La}(t) = i_{La}(t_0)\cos(\omega_a(t-t_0)) + \left(\frac{V_P - V_{Cr} - \frac{nV_O}{2}}{Z_a}\right)\sin\omega_a(t-t_0) \quad (1)$$

$$V_{Cr}(t) = \left(V_P - V_{Ca} - \frac{nV_O}{2}\cos\omega_a(t-t_0)\right) + Z_a i_{La}(t_0)\cos\omega_a(t-t_0) \quad (2)$$

Where, $\omega_a = \frac{1}{\sqrt{L_a C_a}}$;

Characteristic impedance, $Z_a = \sqrt{\frac{L_a}{C_a}}$

Interval (t_1-t_2): This interval begins when MOSFETs S_1,S_4 are turned on, and the primary side voltage, V_p equals to $\frac{nV_o}{2}$. Throughout this interval, energy is transferred to the output load. The equations for i_{La} and V_{Cr} are expressed by (3) and (4).

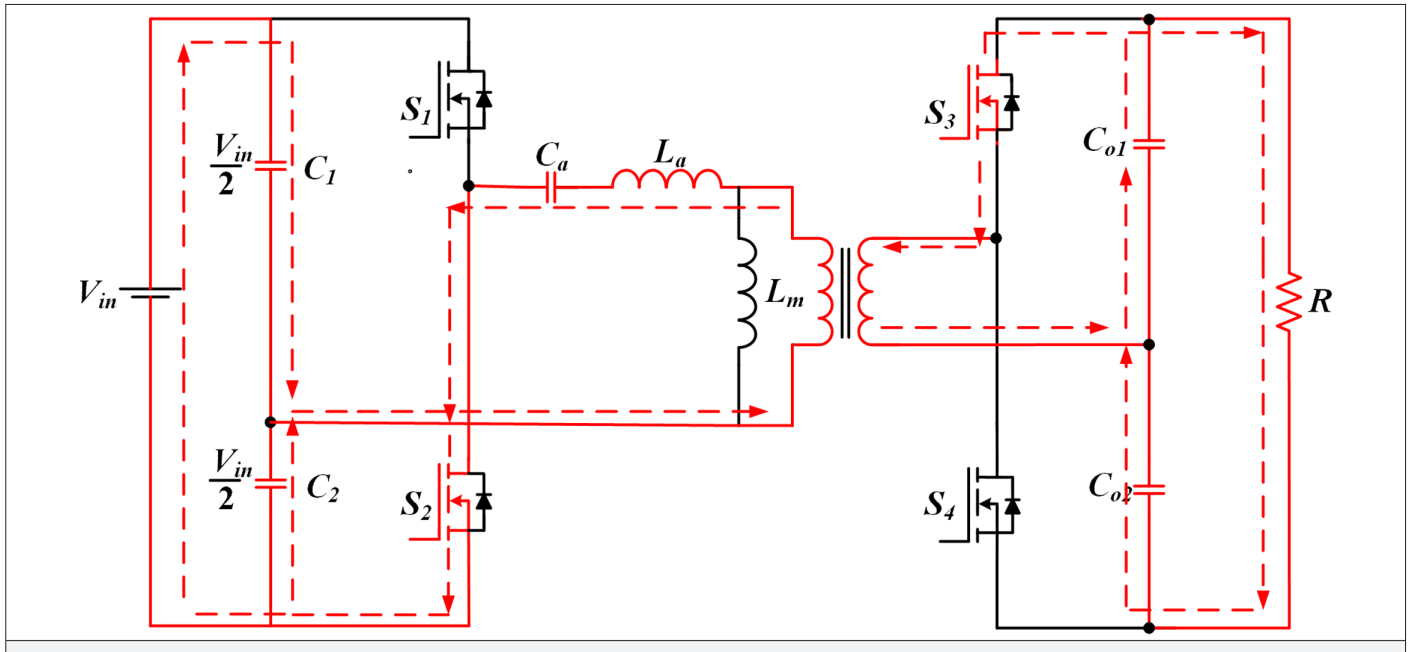

Fig. 7. Equivalent current flow schematic: Interval (t_3-t_4).

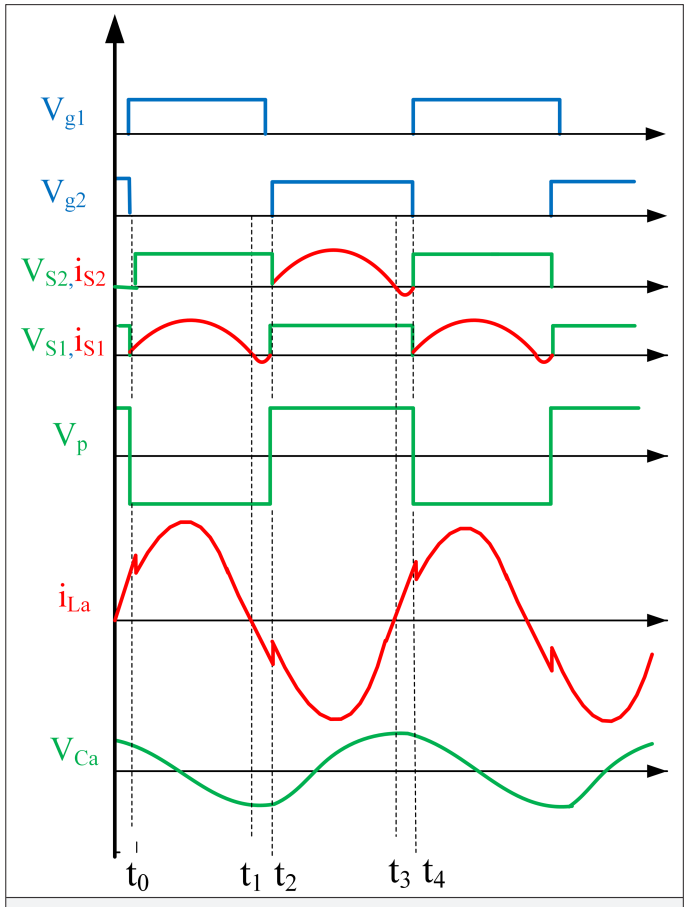

Fig. 8. Key waveforms: ZCS mode.

$$i_{La}(t) = i_{La}(t_1)\cos(\omega_a(t-t_1)) + \left(\frac{V_P - V_{Ca} - \frac{nV_O}{2}}{Z_a}\right)\sin\omega_a(t-t_1) \quad (3)$$

$$V_{Ca}(t) = \left(V_P - V_{Ca} - \frac{nV_O}{2}\cos(\omega_a(t-t_1))\right) + Z_a i_{La}(t_1)\cos\omega_a(t-t_1) \quad (4)$$

Interval (t_2-t_3): This interval begins when S_2, S_3 are gated. The resonant tank current, i_{La} flows through the body diodes of S_2, S_3. The resonant tank current lags with the voltage across V_P the primary side of the transformer. Hence, the ZVS condition is achieved for S_2, S_3. At t_1, body diodes of S_2, S_3 stop conducting.

Interval (t_3-t_4): During this interval, S_2 and S_3 are turned on. Throughout this interval, energy is being transferred to the output load.

B. Zero Current Switching mode

Fig. 8 shows the theoretical waveforms when the operating frequency of the converter is below the resonant frequency. The operation intervals are divided into four intervals. In the first interval (t_0-t_1), at t_0, MOSFETs S_1, S_3 are turned on, and their current flows gradually increase. In this interval, energy is transferred to the load. The second interval (t_1-t_2) is named the resonant interval. During this interval, the resonant current, i_{La} flows and reduces; at the same time, the current through *S1 and* S_3 reaches zero, and then the body diode starts conducting to allow the resonant current, i_{La}. Hence, the ZCS condition is achieved for S_1, S_3. In the interval (t_2-t_3), MOSFETs S_2, S_4 are turned on. Throughout this interval, the energy is transferred to the load. The interval (t_3-t_4) is a resonant interval, the same as (t_1-t_2).

III. DESIGN ANALYSIS

The DAHB converter components are designed by using First Harmonic Analysis (FHA). The equivalent LLC resonant network is shown in Fig. 9. V_{dc} (FHA) is the first harmonic compound expressed by (5), which is the equivalent of the rectangular input voltage of the LLC resonant network. The DAHB converter is analyzed by observing the V_{out} (FHA), the output harmonic compound. The secondary side half-bridge and output load are modeled by a single component R_f (Equivalent resistance) defined in (6).

$$V_{dc}(FHA) = \frac{2V_{in}}{\pi}(2\pi f_s t) \quad (5)$$

$$R_F = \frac{2n^2 V_O}{\pi^2 I_O} \quad (6)$$

Where, n is turns ratio; V_o is output voltage; I_o is output current; f_s is switching frequency

The voltage gain of the DAHB, which is a function of parameters such as switching frequency, load, and components is defined by (7).

$$M = n\frac{V_{out}(FHA)}{V_{dc}(FHA)} = \frac{ky^2}{\sqrt{\left[\left[(k+1)y^2-1\right]^2 + \left[Qky\left(y^2-1\right)\right]^2\right]}} \quad (7)$$

Where

$$k = \frac{L_m}{L_a} \quad (8)$$

Resonant frequency

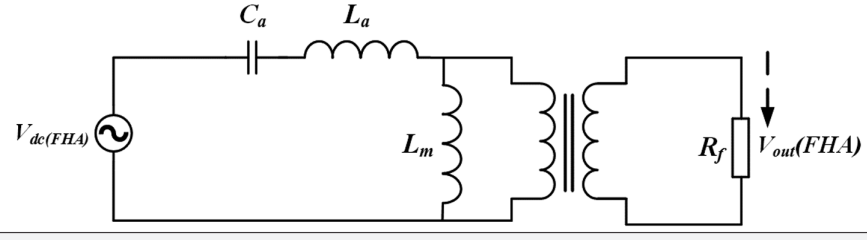

Fig. 9. Equivalent circuit of a resonant network.

$$f_r = \frac{1}{2\pi\sqrt{L_a C_a}} \quad (9)$$

Normalized frequency

$$y = \frac{f_{sw}}{f_r} \quad (10)$$

Quality factor

$$Q = \frac{Z_O}{n^2 R_F} \quad (11)$$

Characteristic impedance

$$Z = \sqrt{\frac{L_a}{C_a}} \quad (12)$$

The parameters of DAHB designed in this section are as follows:

A. Normalized Inductance (k)
Normalized inductance for the DAHB converter is calculated by (8). The obtained normalized inductance value is 14.4 when the DAHB converter is operated at a 100 kHz switching frequency.

B. Magnetizing Inductance (L_m)
The magnetizing inductance value is calculated by (13).

$$L_m = \frac{R_F}{2\pi f_r} \quad (13)$$

The value of magnetizing inductance obtained from the parameters $R_F = 166\,\Omega$ *and* $f_r = 114$ kHz is 231 μH.

C. Resonant inductor (L_a) and Resonant Capacitor (C_a)
The value of resonant inductor, L_a is 15 μH is calculated by the (14)

$$L_a = \frac{L_m}{k} \quad (14)$$

The value of the resonant capacitor, C_a can be calculated by (15).

$$C_a = \frac{1}{\left(2\pi fr\right)^2 L_a} \quad (15)$$

IV. LOSS ANALYSIS

A. Inductor loss
The inductor peak current ($i_{La(peak)}$) is expressed as:

$$i_{La(peak)} = \frac{V_{in}}{2Z_{eq}} \quad (16)$$

Where the characteristic impedance, $Z_{eq} = \sqrt{\frac{L_a}{C_a}}$

The rms current of the inductor ($i_{La(rms))}$ is expressed as

$$i_{La(rms)} = \frac{V_{in}}{2\sqrt{2}Z_{eq}} \quad (17)$$

The rms magnetizing inductor current ($i_{Lm(rms)}$) is given by:

$$i_{Lm(rms)} = \frac{V_{in}}{2\pi f_s \times \sqrt{3} \times L_m} \quad (18)$$

The total rms inductor current ($i_{L(rms)}$) is given by:

$$i_{L(rms)} = \sqrt{i^2_{La(rms)} + i^2_{Lm(rms)}} \quad (19)$$

The copper loss of the inductor ($P_{copper(Loss)}$) can be calculated using (20):

$$P_{copper(Loss)} = i^2_{L(rms)} \times R_{winding} \quad (20)$$

The total core loss of the inductor ($P_{core(Loss)}$) is given by:

$$P_{core(Loss)} = K f_s^{1.6} B_{\max}^{2.3} \times V_{core} \quad (21)$$

Where K = steinmetz constant $= 2.4 \times 10^{-3}$, B_{max} = maximum flux density of the core = 0.427 web/m^2, V_{core} = volume of the core

The total power loss of the inductor ($P_{La(Loss)}$) is given by

$$P_{La(Loss)} = P_{copper} + P_{core} \quad (22)$$

B. Transformer loss
The rms current of the primary winding is expressed as:

$$i_{Tr(primary)} = \frac{i_{peak}}{\sqrt{2}} \quad (23)$$

Where $i_{peak(primary)} = \frac{V_{in}}{2Z_{eq}}$

Transformer copper loss is expressed by

$$P_{copper(Loss)} = \frac{i^2_{peak}}{2}(R_{pri} + n^2 R_{\sec}) \quad (24)$$

Where n = turns ratio, R_{prim} = primary winding resistance, R_{sec} = secondary winding resistance

Transformer core loss is expressed by

$$P_{core(Loss)} = K f_s^{1.6} B_{\max}^{2.3} \times V_{core} \quad (25)$$

Where K=steinmetz constant $= 2.4 \times 10^{-3}$, B_{max} = maximum flux density of the core = 0.1 web/m^2, V_{core} = volume of the core

The total transformer loss is calculated by:

$$P_{Tr(Loss)} = P_{copper} + P_{core} \quad (26)$$

C. Switch losses
The rms current of the primary side switch ($i_{Sp(rms)}$) is given by:

$$i_{Sp(rms)} = \frac{V_{in}}{4 \times \sqrt{2} \times Z_{eq}} \quad (27)$$

The conduction losses ($P_{cond(S1,S2)}$) of the primary side switches are expressed as:

$$P_{cond(S_1,S_2)} = \sum_{p=1}^{2} i^2_{Sp(rms)} \times R_{ds(on)} \quad (28)$$

Where $R_{ds(on)}$=on-state resistance (80 mΩ)

The rms current of the secondary side switch ($i_{Ss(rms)}$) is given by:

$$i_{Ss(rms)} = \frac{nV_{in}}{4 \times \sqrt{2} \times Z_{eq}} \tag{29}$$

The conduction losses (P_{cond}) of the secondary switches are expressed as:

$$P_{cond(S_3,S_4)} = \sum_{s=3}^{4} i_{Ss(rms)}^2 \times R_{ds(on)} \tag{30}$$

Reverse recovery losses of the primary side switches are given by:

$$P_{rr(S_{1-2})} = \sum_{S=1}^{2} Q_{rr} \times V_{ds} \times f_s \tag{31}$$

Where Q_{rr}= reverse recovery charge = $100 \times 10^{0\text{-}1\text{-}2\text{-}3\text{-}4\text{-}5\text{-}6\text{-}7\text{-}8\text{-}9}$coulombs; V_{ds}= voltage across drain to source;

Reverse recovery losses of the secondary-side switches are given by:

$$P_{rr(S_{3-4})} = \sum_{S=3}^{4} Q_{rr} \times V_{ds} \times f_s \tag{32}$$

The gate driver power loss is expressed as

$$P_{Gate(Loss)} = \sum_{S=1}^{4} Q_g \times V_{gs} \times f_s \tag{33}$$

Where Q_g= total gate charge = $120 \times 10^{0\text{-}1\text{-}2\text{-}3\text{-}4\text{-}5\text{-}6\text{-}7\text{-}8\text{-}9}$ coulombs; V_{gs}= voltage across gate-source = 15V

D. Capacitor losses

The effective series resistance (ESR) for the capacitor (C_a) is expressed as:

$$ESR_{Ca} = \frac{\tan\delta}{2\pi f_s C_a} \tag{34}$$

Where $\tan\delta$ is the dissipation factor = 0.0005 radians

$$P_{Loss(Ca)} = i_{Ca(rms)}^2 \times ESR_{Ca} \tag{35}$$

Where the RMS current of capacitor C_a is the same as the RMS current of the resonant inductor L_a

The total power losses in the driver, calculated using (33), are 0.72W. The losses associated with capacitors C_1, C_2, C_3, and C_4 amount to 0.35 W. The reverse recovery losses of the body diodes in switches S_1 and S_2, as determined from (31) and (324), are 3.1W, while those in switches S_3 and S_4 are 4.5W. The total switching power losses, calculated using (28) and (30), which include driver losses and reverse recovery losses of the body diodes, amount to 16.64W. Table I summarizes the overall losses of the converter. Additionally, the inductor loss is 7.2 W, the transformer loss is 6.09 W, and the resonant capacitor loss is 0.57W.

V. EXPERIMENTAL RESULTS

The performance of a discrete SiC MOSFETs-based dual active half-bridge converter is presented in this section. Experimental investigations are performed on the DAHB converter with and without a resonant network, separately. The converter is operated under two conditions: non-resonant and resonant. Firstly, the DAHB converter is assisted with a simple series inductor, *L*, on the primary side of the transformer. It is observed that the SiC MOSFET DAHB converter without series resonant elements operates with partial soft-switching conditions. The parameters used in the experimental analysis are shown in Table II. All operating conditions of the DAHB converter are 330V at 700W maximum output power. The Texas Instruments TMSF28335 microcontroller is used to generate the PWM signals, which are then fed into Infineon's 1EDI30J12CP gate driver to generate the required 100 kHz switching frequency signals for controlling the SiC MOSFETs. Two 1EDI30J12CP drivers are employed in parallel to drive a total of four SiC MOSFETs. In non-resonant mode, the primary side of the DAHB converter without series resonant elements is supplied with 330V input voltage, 1.6 A input current, and 430V output voltage is obtained at 1.2 A output current. Fig. 10 shows SiC MOSFETs S_1, S_2 voltage waveforms across the drain to source and current through the drain. It can be seen from the obtained waveforms that the current flowing through the SiC MOSFETs is different from that of conventional Si MOSFET-based DAHB converters. Soft-switching is achieved when the drain-source voltage reaches zero, and the body diode of SiC MOSFETs S_1, S_2 are conducting without series resonant elements. Fig. 11 shows the waveforms of the transformer primary voltage V_{PQ}, secondary side voltage V_{RS}, and current through i_L. The primary side and secondary side voltage waveforms are identical. The obtained waveforms are very similar to those of conventional Si MOSFET-based dual half-bridge converters. Though the novelty of this SiC MOSFET-based DAHB is without a resonant

TABLE I. LOSS CALCULATION OF THE PROPOSED CONVERTER

Device Type	Components	*Resistance mΩ*	V_{max} (V)	I_{rms} (A)	I_{max} (A)	Loss (W)	Loss Percentage
Switches	S_1, S_2	$R_{ds(on)}$ = 80	165	6	8.5	5.76	54
	S_3, S_4	$R_{ds(on)}$ = 80	250	4	5.65	2.56	
Inductor	L_a	$R_{winding}$ = 15	330	12	17	7.2	23
Transformer	T_r	R_{pri} = 20 R_{sec} = 50	330	12	17	6.08	20
Capacitor	C_a	0.3	330	12	17	0.57	3

TABLE II. PROTOTYPE PARAMETERS

Parameters	Symbol	Value
Input voltage	V_{in}	330V
Output voltage	V_{out}	500V
Switching frequency	f_{sw}	100 kHz
High frequency transformer		SKYVFTR15
Resonant inductor	L_a	20 µH
Resonant capacitor	C_a	200 nF/130 nF
Output capacitor	C_o	470 µF
SiC MOSFETs	S_1-S_4	SCH2080KE

network, it achieves soft commutation during the turn-on of their switching devices.

By adopting L_a and C_a to the primary side of the transformer, experiments are conducted on ZVS and ZCS conditions separately. When the converter is operated below the resonance frequency, DAHB operates in ZVS mode, i.e., at 100 kHz switching frequency and 93 kHz resonant frequency. Experimental waveforms are shown in Fig. 12 the voltage and current waveforms of the SiC MOSFETs S_1, S_2 and Fig. 13 illustrate the voltage waveform across primary and secondary sides of the transformer. Similarly, the converter is operated below the resonance frequency, i.e., 110 kHz. It can be seen from the obtained results that the ZVS turn-on condition is achieved without any additional stresses. Fig. 14 shows the voltage and current waveforms of the SiC MOSFETs S_1, S_2, and Fig. 15 shows the voltage waveform across primary and secondary sides, as well as the current through L_a and the current through secondary side. From these

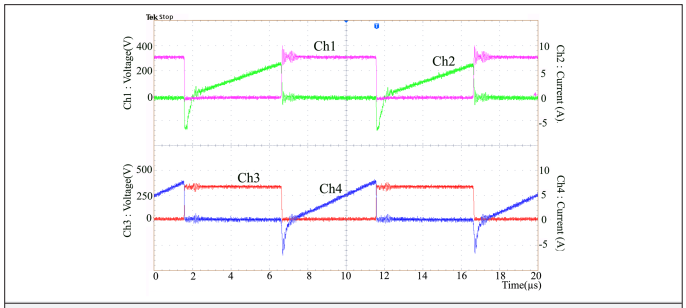

Fig. 10. Experimental waveforms: Non-Resonant mode (a) Ch1 (200V/div): S_1 drain to source voltage Ch2 (5A/div): S_1 Drain current Ch3 (250V/div): S_2 drain to source voltage Ch4 (5A/div): S_2 Drain current.

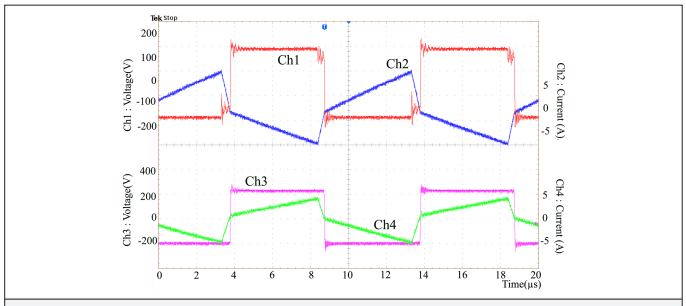

Fig. 11. Experimental waveforms: Non-Resonant mode Ch1 (100V/div) : Transformer primary voltage (upper) Ch2 (5A/div) : Transformer secondary side current (upper) ; Ch3 (200V/div) : Transformer secondary side voltage Ch4 (5A/div) : Transformer secondary side current (bottom).

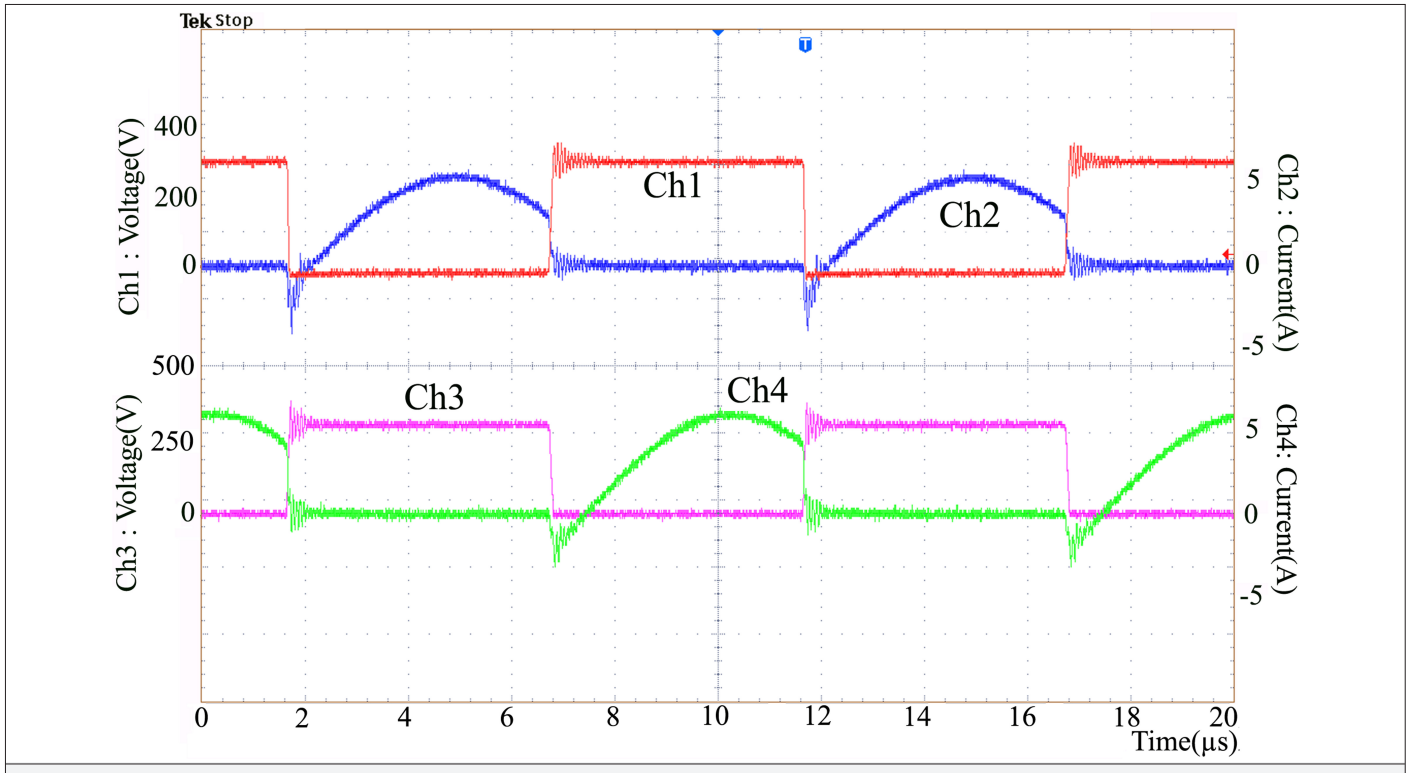

Fig. 12. Experimental waveforms: Resonant mode ZVS Ch1 (200V/div): S_1 Drain to source voltage, of Ch2 (5A/div): S_1 Drain current Ch3 (250V/div): S_2 Drain to source voltage Ch4 (5A/div): S_2 Drain current.

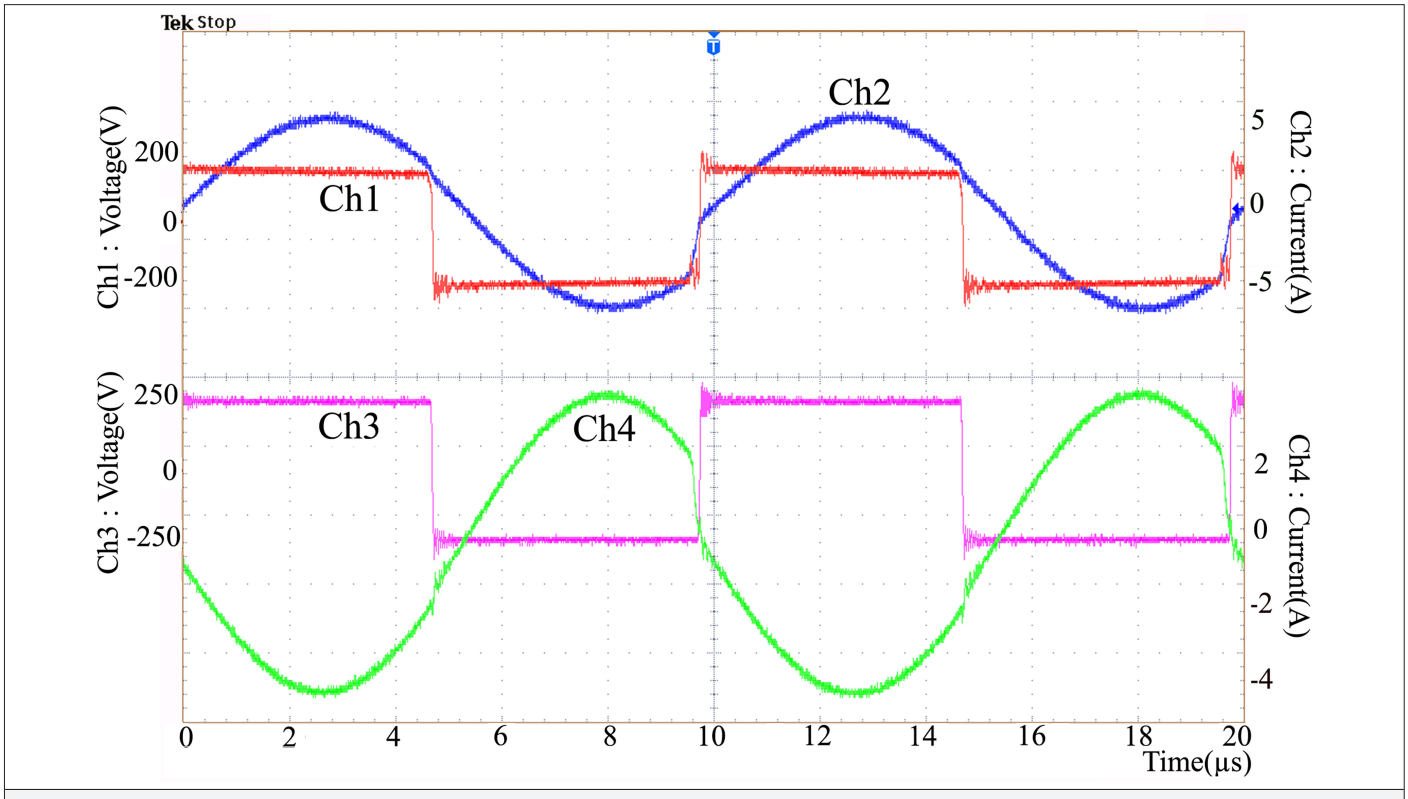

Fig. 13. Experimental waveforms: Resonant mode ZVS): Ch1 (200V/div) : Transformer primary voltage Ch2 (5A/div) : Transformer secondary side current Ch3 (250V/div) : Transformer secondary side voltage Ch4 (2A/div) : Transformer secondary side current.

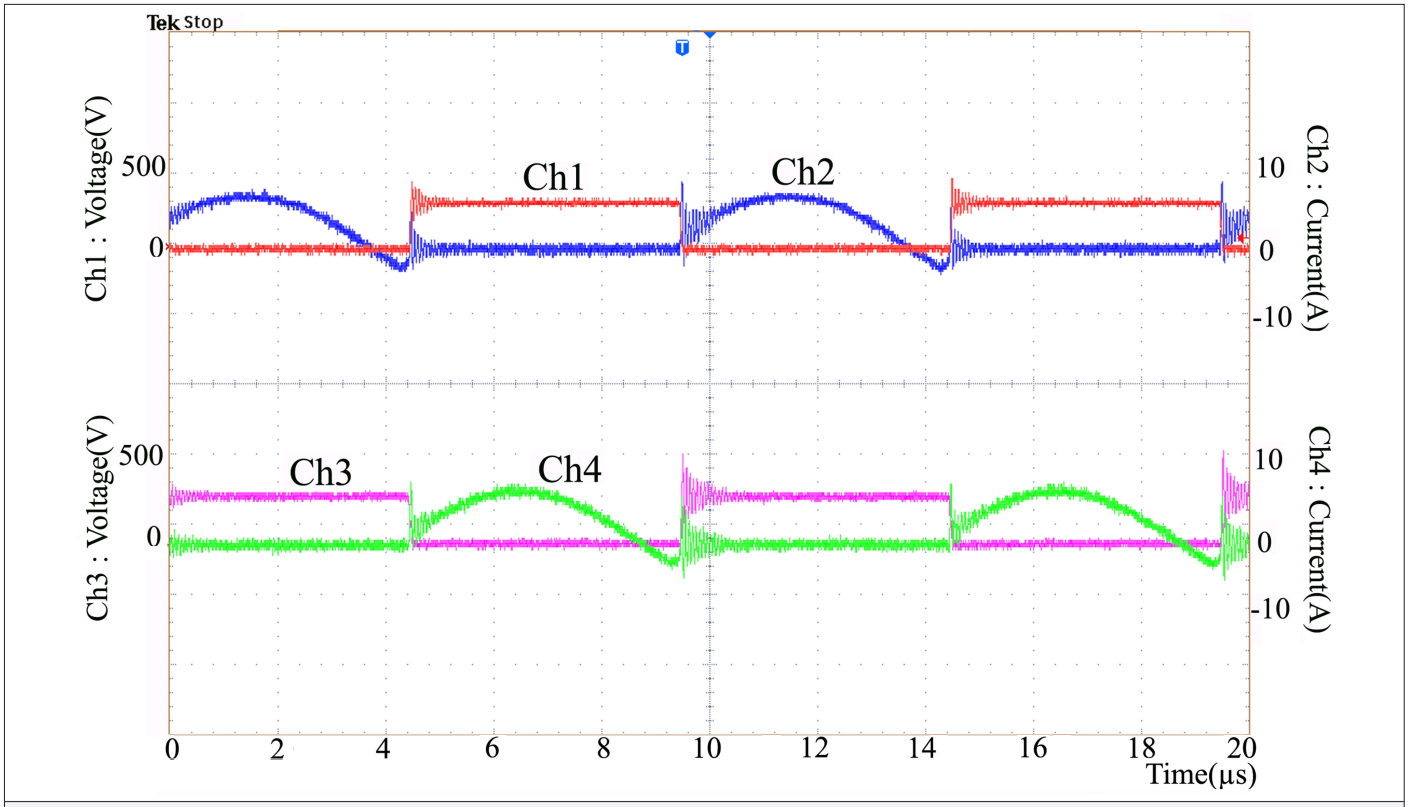

Fig. 14. Experimental waveforms: Resonant mode ZCS Ch1 (200V/div): S_1 Drain-to-source voltage Ch2 (5A/div): S_1 Drain current Ch3 (250V/div): S_2 Drain to source voltage Ch4 (5A/div): S_2 Drain current.

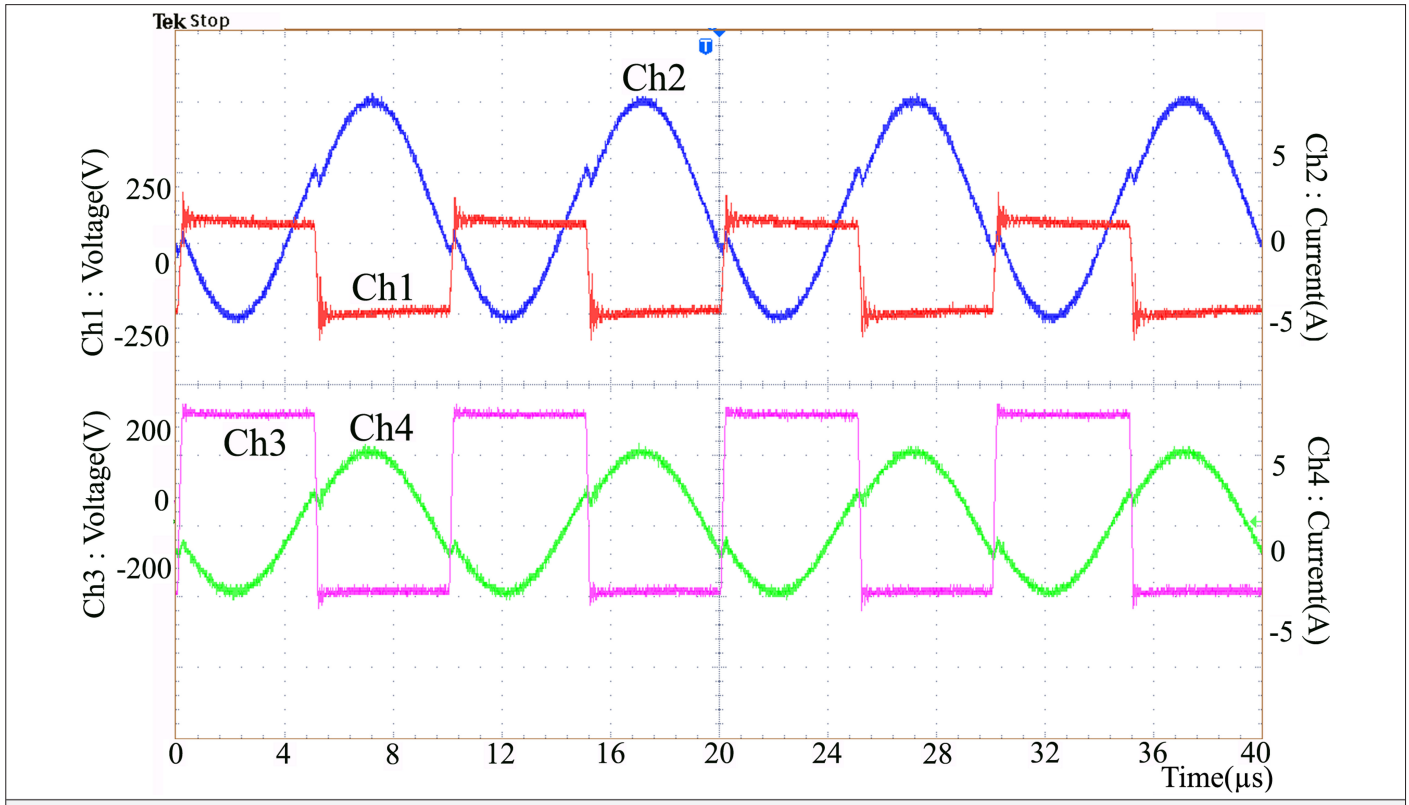

Fig. 15. Experimental waveforms: Resonant mode ZCS Ch1 (200V/div): Transformer primary voltage Ch2 (5A/div) : Transformer secondary side current Ch3 (250V/div) : Transformer secondary side voltage Ch4 (2A/div) : Transformer secondary side current.

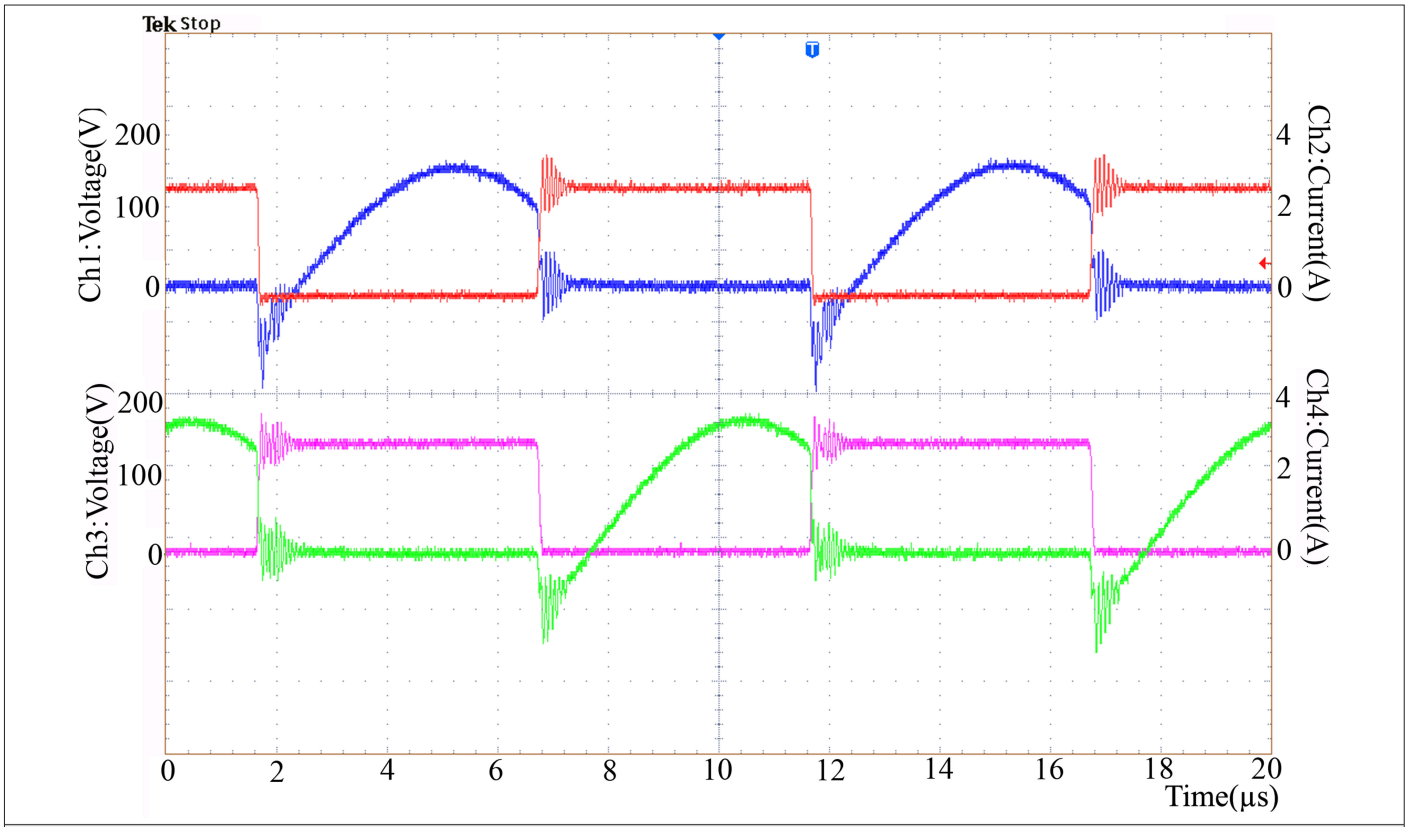

Fig. 16. Turn-on and Turn-off Transitions of the switches S_1, S_2 : ZVS Mode Ch1: 100V/div Ch2: 2A/div, Ch3:100V/div, Ch4: 2A/div , Time: 2 µs/div.

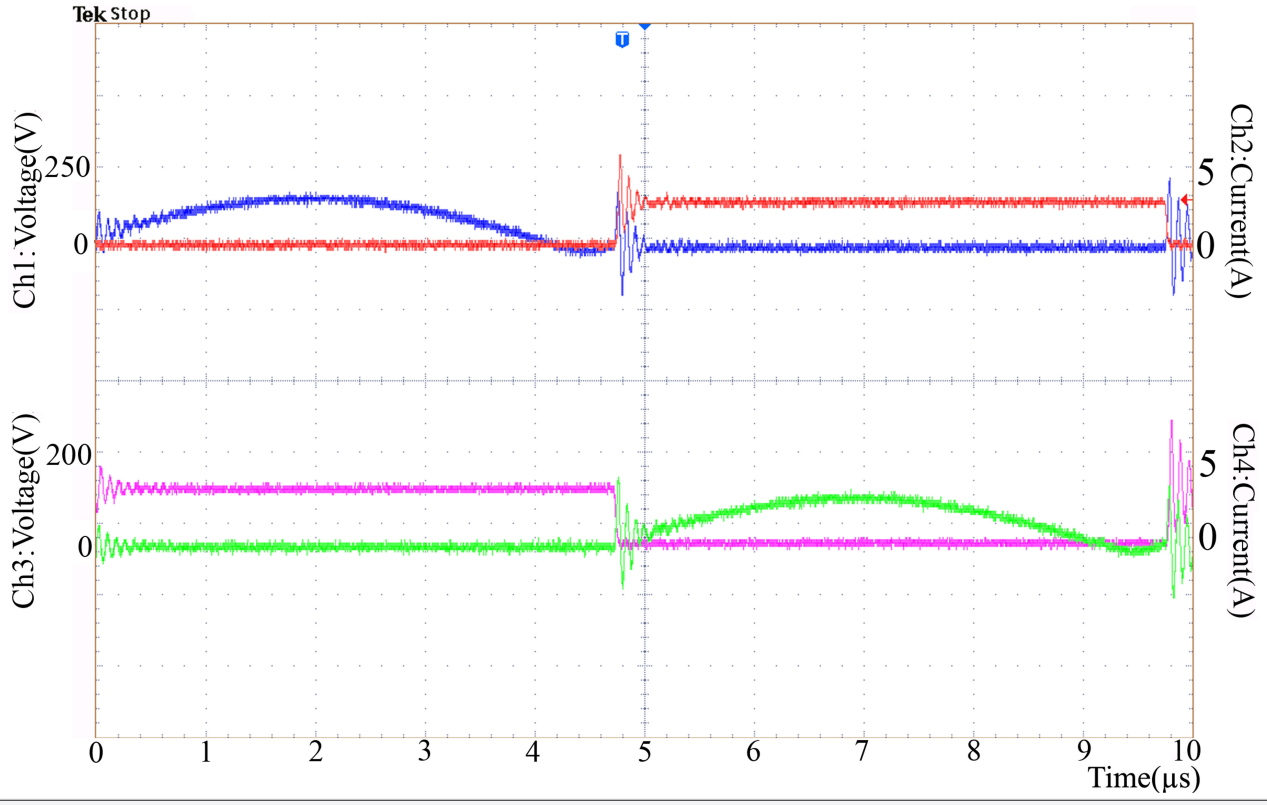

Fig. 17. Turn-on and Turn-off Transitions of the switches S_1, S_2 : ZCS Mode Ch1: 250V/div Ch2: 5A/div, Ch3:200V/div, Ch4: 5A/div Time: 1 µs/div.

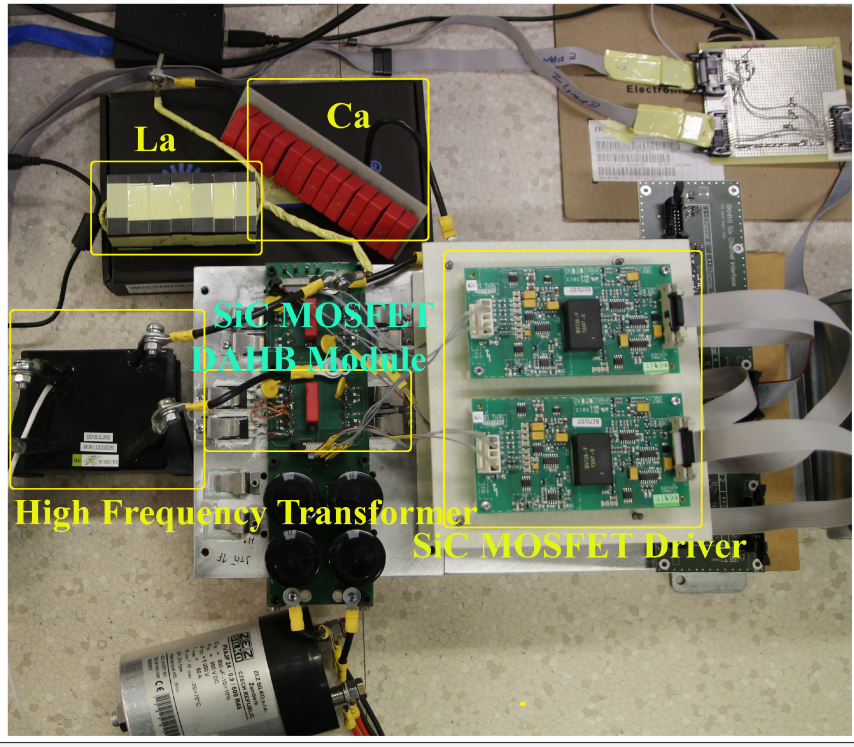

Fig. 18. Photograph of the experimental setup.

results, it is noticed that the ZCS turn-off condition is achieved and is different from that of conventional Si MOSFET-based LLC resonant converter. It is also observed that the body diode of SiC MOSFETs are conducting even before it gets turned off. Fig. 16 shows the turn-on and turn-off transitions of switches S_1 and S_2 in ZVS mode, while Fig. 17 illustrates the corresponding transitions in ZCS mode. From the obtained waveforms, it is evident that the ZVS turn-on operation occurs without any parasitic oscillations. In contrast, during the turn-on instant in ZCS mode, some oscillations appear across the switches due to parasitic effects, and the ZCS turn-off transition of the switches is clearly observed. Fig. 18 shows a photograph of the experimental setup used to conduct the investigations.

A. Efficiency comparison

The efficiency analysis performed on two configurations is presented in this section. The efficiency analysis is made for the proposed converter when the supply voltage is 330V. The complete loss distribution is shown in Fig. 19. At an output power of 700W, the total system losses are 30.8W, yielding an overall efficiency of 96%. Fig. 20 shows efficiency curves of non-resonant and resonant modes (ZVS & ZCS). When the converter is operated at 500 W output power, maximum efficiency for the non-resonant mode is obtained and is 95%. Similarly, when the converter is operating in resonant mode, efficiency in ZVS mode and ZCS mode are compared separately. In ZVS mode, the DAHB is tested at 330V input voltage and the maximum efficiency obtained is 96.5% at 700W output power. An increase of 1% efficiency is observed over the non-resonant mode. In ZCS mode, the DAHB is tested at 330V input voltage and the maximum efficiency obtained is 95.6%.

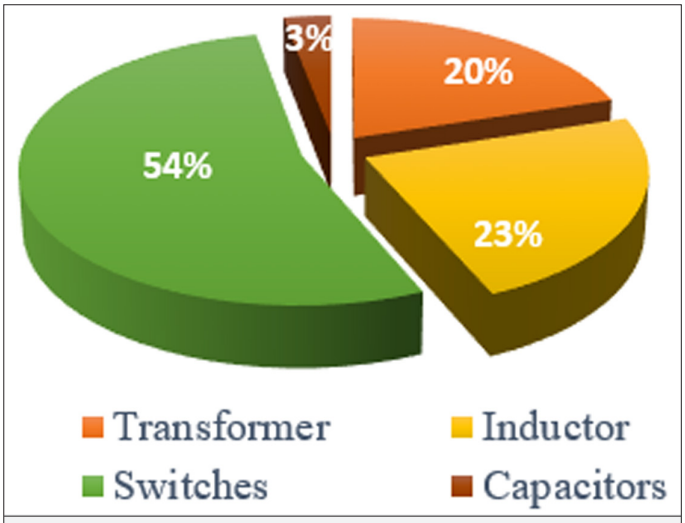

Fig. 19. Loss Distribution

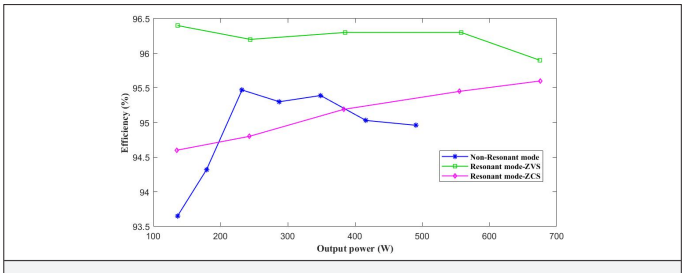

Fig. 20. Efficiency curves.

VI. CONCLUSION

This paper presents the performance of a SiC MOSFET-based DAHB converter under non-resonating and resonating conditions. The operation principles and design analysis are also discussed. The designed converter system operated with a 330V input voltage and achieved a 500V output voltage at 700W output power. This performance analysis was conducted using discrete SiC MOSFETs in both non-resonant and resonant modes. When the converter is operated at 500W output power, the maximum efficiency obtained was 95% in non-resonant mode. The obtained efficiency was 96.5% when the converter was operating in ZVS mode and 96% in ZCS mode, both operating at 700W maximum output power. The obtained efficiencies confirm that the dual half-bridge converter has better efficiency in ZVS mode than in ZCS mode.

Data Availability Statement: The data that support the findings of this study are available upon request from the corresponding author.

Peer-review: Externally peer-reviewed.

Author Contributions: Concept – V.V.S.K.B.; Design – V.V.S.K.B.; Supervision – P.D., V.K.; Resources – P.D.; Materials – P.D.; Data Collection and/or Processing – V.V.S.K.B., P.B.; Analysis and/or Interpretation – V.V.S.K.B., P.B.; Literature Search – V.V.S.K.B.; Writing – V.V.S.K.B.; Critical Review – P.D., V.K.

Declaration of Interests: The authors have no conflicts of interest to declare.

Funding: The authors declare that this study received no financial support.

REFERENCES

1. Y. Xie, J. Sun, and J. S. Freudenberg, "Power flow characterization of a bidirectional galvanically isolated high-power DC/DC converter over a wide operating range," *IEEE Trans. Power Electron.*, vol. 25, no. 1, pp. 54–66, 2010.
2. E. L. Carvalho, C. A. Felipe, L. V. Bellinaso, C. M., d. O. Stein, R. Cardoso, and L. Michels, "Asymmetrical-PWM DAB converter with extended ZVS/ZCS range and reduced circulating current for ESS applications," *IEEE Trans. Power Electron.*, vol. 36, no. 11, pp. 12990–13001, 2021.
3. H. Li, and F. Z. Peng, "Modeling of a new ZVS bi-directional dc-dc converter," *IEEE Trans. Aerosp. Electron. Syst.*, vol. 40, no. 1, pp. 272–283, 2004.
4. J. Kim, H. -S. Song, and K. Nam, "Asymmetric duty control of a dual-half-bridge DC/DC converter for single-phase distributed generators," *IEEE Trans. Power Electron.*, vol. 26, no. 3, pp. 973–982, 2011. [CrossRef]
5. R. de Castro, J. Brembeck, and R. E. Araujo, "Nonlinear control of dual half bridge converters in hybrid energy storage systems," IEEE Vehicle Power and Propulsion Conference (VPPC), Gijon, Spain, 2020, pp. 1–5.
6. S. Chakraborty, and S. Chattopadhyay, "Fully ZVS, minimum RMS Current Operation of the dual-active half-bridge converter using closed-loop three-degree-of-freedom control," *IEEE Trans. Power Electron.*, vol. 33, no. 12, pp. 10188–10199, 2018. [CrossRef]
7. M. Tissières, I. Askarian, M. Pahlevani, A. Rotzetta, A. Knight, and I. Preda, "A digital robust control scheme for dual Half-Bridge DC-DC converters," IEEE Applied Power Electronics Conference and Exposition (APEC), San Antonio, TX, USA, 2018, pp. 311–315. [CrossRef]
8. S. Inoue, M. Ishigaki, A. Takahashi, and T. Sugiyama, "Design of an isolated bidirectional DC–DC converter with built-in filters for high power density," *IEEE Trans. Power Electron.*, vol. 36, no. 1, pp. 739–750, 2021. [CrossRef]
9. Y. Wang *et al.*, "A dual-active-bridge with half-bridge submodules DC solid-state transformer for DC distribution networks," *IEEE J. Emerg. Sel. Top. Power Electron.*, vol. 9, no. 2, pp. 1891–1904, 2021. [CrossRef]
10. K. Kim, and H. Cha, "Split-capacitor dual-active-bridge converter," *IEEE Trans. Ind. Electron.*, vol. 68, no. 2, pp. 1445–1453, 2021. [CrossRef]
11. A. Aghajani, N. Zare Kashani, M. Eldoromi, and A. A. M. Birjandi, *"A Novel Half-Full-Bridge Split-Capacitor DC-DC Converter Based On Dual-Active-Bridge Topology," 13th Power Electronics, Drive Systems, and Technologies Conference (PEDSTC)*. Tehran, Iran, 2022, pp. 240–244.

12. V. Esteve, J. L. Bellido, J. Jordán, and E. J. Dede, "Improving the efficiency of an isolated bidirectional dual active bridge DC–DC converter using variable frequency," *Electronics*, vol. 13, no. 2, 2024. [CrossRef]
13. M. Su, J. Huang, H. Wang, L. Jiang, and X. Chen, "Direct AC–AC solid-state transformer based on hybrid DAB," *IEEE J. Emerg. Sel. Top. Power Electron.*, vol. 12, no. 2, pp. 1385–1394, 2024. [CrossRef]
14. A. A. Nkembi *et al.*, "A novel feedforward scheme for enhancing dynamic performance of vector-controlled dual active bridge converter with dual phase shift modulation for fast battery charging systems," *Electronics*, vol. 13, no. 19, 2024. [CrossRef]
15. Q. -X. Guan, Y. Zhang, H. -B. Zhao, and Y. Kang, "Optimized switching strategy for ANPC–DAB converter through multiple zero states," *IEEE Trans. Power Electron.*, vol. 37, no. 3, pp. 2885–2898, 2022. [CrossRef]
16. S. Goudarzitaemeh, L. Melanson, J. Woelfle, and M. Pahlevani, "A multi-level current-fed DAB converter with direct power transfer," *IEEE Open J. Power Electron.*, vol. 5, pp. 1612–1628, 2024. [CrossRef]
17. L. Li, M. Su, G. Xu, L. Jiang, and Y. Liu, "A soft-switched semi dual active half bridge converter with voltage match trapezoidal modulation control," *IEEE Trans. Circuits Syst. II*, vol. 72, no. 1, pp. 303–307, 2025. [CrossRef]
18. K. R and R. Kalpana, "An isolated dual-input half-bridge DC–DC boost converter with reduced circulating power between input ports," *Can. J. Electr. Comput. Eng.* New York: IEEE, vol. 45, no. 1, pp. 68–76, 2022.
19. J. Zhang, Y. Tang, W. Hu, Z. Zhang, J. Li, and Z. Chen, "Minimum current stress operation of dual active half-bridge converter using triple phase shift control for renewable energy applications," *Energy Rep.*, vol. 8, pp.547–553, 2022. [CrossRef]
20. N. Sachdev, and A. K. S. Bhat, "Performance comparison of Si and SiC MOSFETs in a bidirectional dual half-bridge series resonant converter," International Conference on Power, Instrumentation, Control and Computing (PICC), Thrissur, India, 2018, pp. 1–6.

Veera Venkata Subrahmanya Kumar Bhajana received his B.E. in Electronics and Communication Engineering from Sapthagiri College of Engineering, India (University of Madras), in 2000, his M.E. from the P.S.N.A College of Engineering and Technology under Anna University in 2005, and PhD in Electrical Engineering from Bharath University, India, in 2011. He was previously associated as a post-doctoral researcher at the University of West Bohemia, Pilsen, Czech Republic, from August 2013 to June 2015. He is currently working as an Associate Professor in the School of Electronics Engineering at KIIT (Kalinga Institute of Industrial Technology) University, Bhubaneswar, India, since December 2011.

Pravat Biswal was born in Bhubaneswar, India. He received the B.Tech. degree in electrical engineering from the C.V. Raman College of Engineering in Bhubaneswar, Odisha, India, in 2008, and the M.Tech. degree from NIT Warangal, specializing in power electronics and drives, in 2011. He is currently a Ph.D. Research Scholar and an Assistant Professor with KIIT University, Odisha.

Pavel Drabek received his M.S. and PhD degrees in electrical in electrical engineering from the University of West Bohemia (UWB), Pilsen, Czech Republic, in 2000 and 2004, respectively. From 2003 to 2005, he was a Design Engineer with the company Alltronic, Ltd., Pilsen. In 2005, he joined UWB as an Assistant Professor in the department of Electromechanics and Power Electronics, Faculty of Electrical Engineering. His main research interests include soft-switching inverters, AC-AC converters, multilevel converters, and electromagnetic compatibility of power electronic converters.

VIJAY KAKANI received the B.Sc. degree in electronics and communication engineering from Jawaharlal Nehru Technological University, Kakinada, India, in 2012, the M.Sc. degree in computers and communication systems from the University of Limerick, Ireland, in 2014, and the Ph.D. degree in information and communication engineering and future vehicle engineering from Inha University, South Korea, in 2020. He is currently an Assistant Professor in the Department of Integrated System Engineering, School of Global Convergence Studies, Inha University. His research interests include autonomous vehicles, sensor signal processing, applied computer vision, deep learning, systems engineering, and machine vision applications.